

A helium-burning white dwarf binary as a supersoft X-ray source

J. Greiner¹, C. Maitra¹, F. Haberl¹, R. Willer¹, J.M. Burgess¹, N. Langer^{2, 3},
J. Bodensteiner⁴, D.A.H. Buckley^{5, 6, 7}, I.M. Monageng⁵, A. Udalski⁸,
H. Ritter⁹, K. Werner¹⁰, P. Maggi¹¹, R. Jayaraman¹², and R. Vanderspek¹²

¹*Max-Planck Institut für Extraterrestrische Physik, 85748 Garching, Giessenbachstr. 1, Germany*

²*Argelander-Institut für Astronomie, Universität Bonn, Auf dem Hügel 71, 53121 Bonn, Germany*

³*Max-Planck-Institut für Radioastronomie, Auf dem Hügel 69, 53121, Bonn, Germany*

⁴*ESO – European Organisation for Astronomical Research in the Southern Hemisphere, 85748 Garching, Karl-Schwarzschild-Str. 2, Germany*

⁵*South African Astronomical Observatory, PO Box 9, Observatory Rd, Observatory 7935, South Africa*

⁶*Department of Astronomy, University of Cape Town, Private Bag X3, Rondebosch 7701, South Africa*

⁷*Department of Physics, University of the Free State, PO Box 339, Bloemfontein 9300, South Africa*

⁸*Astronomical Observatory, University of Warsaw, Al. Ujazdowskie 4, 00-478 Warszawa, Poland*

⁹*Max-Planck Institut für Astrophysik, 85748 Garching, Karl-Schwarzschild-Str. 1, Germany*

¹⁰*Institut für Astronomie und Astrophysik, Kepler Center for Astro and Particle Physics, Universität Tübingen, 72076 Tübingen, Sand 1, Germany*

¹¹*Université de Strasbourg, CNRS, Observatoire astronomique de Strasbourg, UMR 7550, F-67000 Strasbourg, France*

¹²*Department of Physics and Kavli Institute for Astrophysics and Space Research, Massachusetts Institute of Technology, 70 Vassar St., Cambridge, MA 02139, USA*

March 24, 2023

Type Ia supernovae are cosmic distance indicators^{1;2}, and the main source of iron in the Universe^{3;4}, but their formation paths are still debated. Several dozen supersoft X-ray sources, in which a white dwarf accretes hydrogen-rich matter from a non-degenerate donor star, have been observed⁵ and suggested as Type Ia supernovae progenitors^{6;7;8;9}. However, observational evidence for hydrogen, which is expected to be stripped off the donor star during the supernova explosion¹⁰, is lacking. Helium-accreting white dwarfs, which would circumvent this problem, have been predicted for more than 30 years^{7;11;12}, also including their appearance as supersoft X-ray sources, but have so far escaped detection. Here we report a supersoft X-ray source with an accretion disk whose optical spectrum is completely dominated by helium, suggesting that the donor star is hydrogen-free. We interpret the luminous and supersoft X-rays as due to helium burning near the surface of the accreting white dwarf. The properties of our system provides evidence for extended pathways towards Chandrasekhar mass explosions based on helium accretion, in particular for stable burning in white dwarfs at lower accretion rates than expected so far. This may allow to recover the population of the sub-energetic so-called Type Iax supernovae, up to 30% of all Type Ia supernovae¹³, within this scenario.

The X-ray source [HP99] 159¹⁴ has been seen since the early 1990s with ROSAT, XMM-*Newton* (4XMM J052015.1–654426) and recently eROSITA (eRASSU J052015.3-654429) with a very soft spectrum (effective blackbody temperature of $kT = 45 \pm 3$ eV, or 522 ± 35 kK; Fig. 1). Using the 1''-accurate XMM X-ray position, we identify [HP99] 159 with a 16 mag object at RA (2000.0) = $05^{\text{h}}20^{\text{m}}15^{\text{s}}.50$, Decl. (2000.0) = $-65^{\circ}44'27''.1$. An optical spectrum taken with the Robert Stobie Spectrograph (RSS) at the Southern African Large Telescope (SALT) shows a wealth of emission lines (Fig. 2), all shifted by the Large Magellanic Cloud (LMC) systemic velocity¹⁵ of 262.2 ± 3.4 km s⁻¹, indicating that the source is indeed situated at LMC distance (50 kpc¹⁶). Thus, the X-ray fit leads to a high bolometric luminosity of $6.8_{-3.5}^{+7.0} \times 10^{36}$ erg/s. The corresponding blackbody radius is 3700_{-1900}^{+3900} km, consistent with a white dwarf. This classifies [HP99] 159 as bona-fide supersoft X-ray source^{17;18;5}.

The optical spectrum is unique, in that it shows predominantly He I and He II emission lines (Fig. 2). There are no indications for Balmer lines (see inserts in Fig. 2), no absorption lines typical for a main-sequence star, and no indications either for C or O as seen in Wolf-Rayet stars. The only other emission lines we identify (ED Fig. 2) are 7 lines of NII (5001.5, 5666.6, 5679.6, 6482.0, 6610.6 Å) and SiIII (6347.1, 6371.4 Å). While such lines are typically seen in AM CVn stars, several facts argue against such an interpretation. We find no evidence in the extracted 2D long-slit spectrum of any extended nebulous emission. The strong continuum emission argues against an HII-like region of a (He-rich) planetary nebula.

High-resolution optical spectra taken at 3 epochs with the HRS (High Resolution Spectrograph) at SALT reveal a double-peaked profile of all lines (Fig. 3), thus demonstrating their origin in an accretion disk. With the theoretical maximum intensity of an accretion disk line profile coming from the area of ≈ 0.95 of its maximum Doppler velocity, and assuming Keplerian rotation, we infer a projected velocity of the outer disk of $v_K \times \sin(i) \approx 60$ km s⁻¹. This suggests that the disk is seen at a low inclination angle, close to face-on. Interestingly, the He II lines have a similar profile. The FWZI (full width at zero intensity) in the He I lines suggests a maximum projected velocity of 120 ± 10 km/s, with that of the He II 4686 line clearly being different, about 200 ± 20 km/s.

The accretion disk is not only the origin of the emission lines, but also of the UV-optical-NIR continuum emission, as indicated by its luminosity and spectral slope; the accreting white dwarf and the donor are both hidden under this disk flux. Optical photometry shows periodic variations by a factor of 1.3, with little color variation (see ED Fig. 3). A Lomb-Scargle periodogram shows the largest power at a period of 1.1635 days, and a secondary lower-power peak at 2.327 days. The folded light curve for this longer period has a lower variance and a clear odd-even asymmetry. Phase-resolved spectroscopy is certainly needed to firmly establish which one is the true orbital period.

The helium-dominated accretion disk has two consequences: First, the donor star must be in an evolutionary phase where all the hydrogen is lost. An intriguing option is a helium star

donor, with the nitrogen lines providing evidence for CNO-processed matter from the donor. Secondly, we interpret the high X-ray luminosity as due to steady He burning in a shell on the white dwarf (accretor) surface. Similar to the steady H-shell burning in the canonical supersoft X-ray sources^{19;20}, models of accreting white dwarfs predict a narrow range of accretion rates, with a canonical value of $\sim 10^{-6} M_{\odot}/\text{yr}$, at which He-shell burning is steady^{11;12;7;8;21;22;23}. If the accretion rate is higher, the accreted material puffs up and forms an envelope around the WD which becomes similar to a red giant, likely leading to common envelope evolution. If the accretion rate is lower, burning in the accreted He-layer is unstable, i.e., first starting to oscillate and then leading to He shell flashes that increase the luminosity temporarily by factors of 10 or more, on timescales which depend on various parameters^{24;25}. Even lower accretion rates result in explosive helium burning.

While the measured X-ray temperature is exactly in the range expected for steady He shell burning, our measured luminosity is about ten times smaller than expected for accretion at the canonical rate. At the same time, the historical X-ray light curve, from *Einstein* (1979) and EXOSAT limits (1984–1986) to the ROSAT detection in 1992, and the XMM-*Newton* and eROSITA detections since 2019, suggests that the luminosity of [HP99] 159 is stable to within a factor of 5 (relative to the XMM-*Newton* value) for nearly 50 years (ED Fig. 5). This indicates the possibility that helium accretion at rates well below the canonical one (i.e., $\approx 10^{-6} M_{\odot}/\text{yr}$) can still lead to stable helium burning.

Stable burning at low accretion rates has been suggested for the case that the accreting white dwarf is rapidly rotating^{24;26}. In corresponding models, stable burning is found²¹ down to $5 \times 10^{-7} M_{\odot}/\text{yr}$, and even for $3 \times 10^{-7} M_{\odot}/\text{yr}$ when allowing for fluctuations of the burning rate of a factor three. In the latter situation, the X-ray luminosity at any given time may be up to a factor of three smaller, or larger, than the value deduced from a given accretion rate assuming strictly stationary burning. If [HP99] 159 were currently near a luminosity minimum, which is more likely than it being near a maximum, its helium accretion rate could indeed be as high as $3 \times 10^{-7} M_{\odot}/\text{yr}$. While we can not exclude that the burning rate of [HP99] 159 is oscillating with a growing amplitude, leading to instability, the expected short timescale of the evolution renders this unlikely.

A lower than the canonical burning rate is consistent with our optical spectra. If the accretion rate in [HP99] 159 would be significantly higher, a wind from the white dwarf is expected²⁷. This would manifest itself with emission lines, broadened by the wind velocity (of order thousands km/s). Such broadened lines are not detected.

We have the following constraints on the mass of the He star: For initial He-star masses above $\approx 1 M_{\odot}$, long-term stable evolution has been found⁹. The maximum possible initial mass depends on the assumptions concerning the wind. The present mass could be smaller than that. A rough upper bound on the present mass could be derived using the constraint that its luminosity is obviously smaller than that of the accretion disk. A helium star luminosity below

$\approx 1000 L_{\odot}$ implies²⁸ that the current mass of the helium star is smaller than $\approx 2 M_{\odot}$.

An orbital period of (1.16 d) 2.32 d suggests that the He star fills its Roche lobe radius of $\approx(3) 4 R_{\odot}$, being about a factor of 10 larger than on the He main sequence. In this picture, as long as the mass of the He star donor is larger than that of the white dwarf accretor, mass transfer will proceed on the thermal timescale ($\approx 10^5 \dots 10^6$ yrs), reducing the separation of the stars. Indeed, for He stars in the $0.8\text{--}2 M_{\odot}$ range (corresponding to initial masses on the main-sequence of $4\text{--}8 M_{\odot}$), this thermal timescale mass transfer²⁹ (during their sub-giant or giant phases) is predicted to reach rates of order $10^{-7} \dots 10^{-5} M_{\odot}/\text{yr}$, allowing for stable He burning. After mass ratio inversion, the mass transfer rate drops and the binary widens. This may lead to the weak He-shell flash regime, consistent with [HP99] 159.

Various scenarios of white dwarfs accreting matter from a helium star companion have been suggested to lead to Type Ia supernovae. At the lowest accretion rates, helium can pile up on the white dwarf and lead to a sub-Chandrasekhar mass explosion after a critical amount of mass has been accumulated. However, in [HP99] 159 the X-ray emission implies continuous burning of the accreted matter, and consequently a continuous growth of the white dwarf mass. For this case, it has been suggested that the white dwarf undergoes a Type Ia supernova explosion once the Chandrasekhar mass is reached. A standard Type Ia explosion may strip $2 \dots 5\%$ of the mass of the helium star³⁰, of which no signature has been observed so far. However, it has been suggested that Chandrasekhar mass WDs may undergo sub-energetic deflagrations³¹, leading to subluminous so-called Type Iax supernovae, which are expected to strip off about ten times less mass from their helium donors³². Weak helium lines have been observed in the spectra of two Type Iax supernovae¹³, and a helium donor star has been proposed for the Type Iax SN 2012Z based on deep pre-explosion imaging³³. The recent detection of helium in the bright Type Ia SN 2020eyj³⁴ indicates that helium donors may also sometimes trigger energetic white dwarf explosions.

While we do not know whether [HP99] 159 will evolve into a Type Ia supernova, its properties provide evidence for the pathway towards Chandrasekhar mass explosions based on helium accretion being wider than thought before. Its X-ray luminosity of $\sim 1800 L_{\odot}$ corresponds to a stationary helium accretion rate of $1.5 \cdot 10^{-7} M_{\odot}/\text{yr}$, for which many models currently predict unstable burning²⁶. However, [HP99] 159 appears to be relatively stable within the last 50 yr. Stable burning for lower accretion rates, as perhaps enabled by rapid rotation²¹, may allow lower mass donors to push their companion WDs to the Chandrasekhar mass. This may allow us to recover the SN Iax population within this scenario, which makes up about 30% of all Type Ia supernovae¹³. Folding our constraint on the radius of the WD in [HP99] 159 with a WD mass-radius relation³⁵, we find a current WD mass of $1.20^{+0.18}_{-0.40} M_{\odot}$, implying that [HP99] 159 could undergo a Type Iax supernova explosion in the future.

When we assume that $\approx 10\%$ of all Type Ia supernovae in our Galaxy ($\approx 10^{-3}$ per year⁹) follow the path of helium accretion leading to Type Iax explosions, and adopting a lifetime of

3×10^5 yrs (assuming $0.3 M_{\odot}$ need to be transferred at $10^{-6} M_{\odot}/\text{yr}$), we predict about 30 helium accreting supersoft X-ray sources presently in the Milky Way. Scaling with the star formation rate would yield a handful of systems in the LMC. The detection and study of more of these sources will likely allow us to tighten the constraints on the single degenerate progenitor channel for Type Ia supernovae.

References

- [1] Elias, J.H., Matthews, K., Neugebauer, G., Persson, S.E., Type I supernovae in the infrared and their use as distance indicators. *Astrophys. J.* **296**, 379–389 (1985)
- [2] Riess, A.G., Press, W.H., Kirshner, R.P., A Precise Distance Indicator: Type IA Supernova Multicolor Light-Curve Shapes. *Astrophys. J.* **473**, 88–109 (1996)
- [3] Hoyle, F., The synthesis of the elements from hydrogen. *Mon. Not. R. Astron. Soc.* **016**, 343–383 (1946)
- [4] Burbidge, E.M., Burbidge, G.R., Fowler, W.A., Hoyle, F., Synthesis of the Elements in Stars. *Rev. Mod. Phys.* **29**, 547–650 (1957)
- [5] Greiner, J., Catalog of supersoft X-ray sources. *New Astron.* **5**, 137–141 (2000)
- [6] Whelan, J., Iben, I. Jr, Binaries and Supernovae of Type I. *Astrophys. J.* **186**, 1007 (1973)
- [7] Iben, I. Jr., Tutukov, A.V., Helium-accreting Degenerate Dwarfs as Presupernovae and Scenarios for the Ultrasoft X-Ray Sources. *Astrophys. J.* **431**, 264–272 (1994)
- [8] Yoon, S.-C., Langer, N., The first binary star evolution model producing a Chandrasekhar mass white dwarf. *Astron. Astrophys.* **412**, L53–L56 (2003)
- [9] Wang, B., Meng, X., Chen, X., Han, Z. The helium star donor channel for the progenitors of Type Ia supernovae. *Mon. Not. R. Astron. Soc.* **395**, 847–854 (2009)
- [10] Wheeler, J.C., Lecar, M., McKee, C.F., Supernovae in binary systems. *Astrophys. J.* **200**, 145–157 (1975)
- [11] Kawai, Y., Saio, H., Nomoto, K., Steady State Models of White Dwarfs Accreting Helium or Carbon/Oxygen-rich Matter. *Astrophys. J.* **328**, 207–212 (1988)
- [12] Iben, I. Jr., Tutukov, A.V., Model Stars with Degenerate Dwarf Cores and Helium-burning Shells: A Stationary-burning Approximation. *Astrophys. J.* **342**, 430–448 (1989)
- [13] Foley, R.J., Challis, P.J., Chornock, R., Ganeshalingam, M., Li, W., et al. Type Iax Supernovae: A New Class of Stellar Explosion. *Astrophys. J.* **767**, id. 57 (2013)
- [14] Haberl F., Pietsch W., A ROSAT PSPC catalogue of X-ray sources in the LMC region. *Astron. Astrophys. Suppl. Ser.* **139**, 277 (1999)
- [15] van der Marel, R.P., Alves, D.R., Hardy, E., Suntzeff, N.B. New Understanding of Large Magellanic Cloud Structure, Dynamics, and Orbit from Carbon Star Kinematics. *Astron. J.* **124**, 2639–2663 (2002)
- [16] Pietrzynski, G., Graczyk, D., Gellenne, A. A distance to the Large Magellanic Cloud that is precise to one per cent. *Nature* **567**, 200–203 (2019)
- [17] Greiner, J., Hasinger, G., Kahabka, P. ROSAT observation of two supersoft sources in the Large Magellanic Cloud. *Astron. Astrophys.* **246**, L17–L20 (1991)
- [18] van den Heuvel, E.P.J., Bhattacharya, D., Nomoto, K., Rappaport, S.A., Accreting white dwarf models for CAL 83, CAL 87 and other ultrasoft X-ray sources in the LMC. *Astron. Astrophys.* **262**, 97–105 (1992)
- [19] Nomoto, K. Accreting white dwarf models for type I supernovae. I. Presupernova evolution

- and triggering mechanisms. *Astrophys. J.* **253**, 798–810 (1982)
- [20] Fujimoto, M.Y. A Theory of Hydrogen Shell Flashes on Accreting White Dwarfs. II. The Stable Shell Burning and the Recurrence Period of Shell Flashes. *Astrophys. J.* **257**, 767–779 (1982)
- [21] Yoon, S.-C., Langer, N., Scheithauer, S., Effects of rotation on the helium burning shell source in accreting white dwarfs. *Astron. Astrophys.* **425**, 217–228 (2004)
- [22] Piersanti, L., Tornambé, A., Yungelson L.R., He-accreting white dwarfs: accretion regimes and final outcomes. *Mon. Not. R. Astron. Soc.* **445**, 3239–3262 (2014)
- [23] Wong T.L.S., Schwab, J., Götzberg, Y. Pre-Explosion Properties of Helium Star Donors to Thermonuclear Supernovae. *Astrophys. J.* **922**, id. 241 (2021)
- [24] Yoon, S.-C., Langer, N., Helium accreting CO white dwarfs with rotation: Helium novae instead of double detonation. *Astron. Astrophys.* **419**, 645–652 (2004)
- [25] Brooks, J., Bildsten, L., Schwab, J., Paxton, B., Carbon Shell or Core Ignitions in White Dwarfs Accreting from Helium Stars. *Astrophys. J.* **821**, id. 28 (2016)
- [26] Wong, T.L.S., Schwab, J., Evolution of Helium Star-White Dwarf Binaries Leading up to Thermonuclear Supernovae. *Astrophys. J.* **878**, id. 100 (2019)
- [27] Kato, M., Hachisu, I. A New Estimation of Mass Accumulation Efficiency in Helium Shell Flashes toward Type IA Supernova Explosions. *Astrophys. J.* **513**, L41 (1999)
- [28] Langer, N. Standard models of Wolf-Rayet stars. *Astron. Astrophys.* **210**, 93–113 (2019)
- [29] Delgado, A.J., Thomas, H.-C. Mass transfer in a binary system - The evolution of the mass-giving helium star. *Astron. Astrophys.* **96**, 142–145 (1981)
- [30] Liu, Z.-W., Pakmor, R., Seitenzahl, I.R., Hillebrandt, W., Kromer, M. et al. The Impact of Type Ia Supernova Explosions on Helium Companions in the Chandrasekhar-mass Explosion Scenario. *Astrophys. J.* **774**, id. 37 (2013)
- [31] Kromer, M., Fink, M., Stanishev, V., Taubenberger, S., Ciaraldi-Schoolman, F., et al. 3D deflagration simulations leaving bound remnants: a model for 2002cx-like Type Ia supernovae. *Mon. Not. R. Astron. Soc.* **429**, 2287–2297 (2013)
- [32] Zeng, Y., Liu, Z.-W., Han, Z. The Interaction of Type Iax Supernova Ejecta with a Helium Companion Star. *Astrophys. J.* **898**, id. 12 (2020)
- [33] McCully, C., Jha, S.W., Foley, R.J., Bildsten, L., Fong, W.-F., et al. A luminous, blue progenitor system for the type Iax supernova 2012Z. *Nature* **512**, 54–56 (2014)
- [34] Kool, E.C., Johansson, J., Sollerman, J., Moldón, J., Moriya, T.J., et al., A radio-detected thermonuclear supernova from a single-degenerate progenitor with a helium star donor. *Nature* (subm.; arXiv:2210.07725) (2022)
- [35] Rotondo, M., Rueda, J.A., Ruffini, R., Xue, S.-S. Relativistic Feynman-Metropolis-Teller theory for white dwarfs in general relativity. *Phys. Rev. D* **84**, id. 084007 (2011)

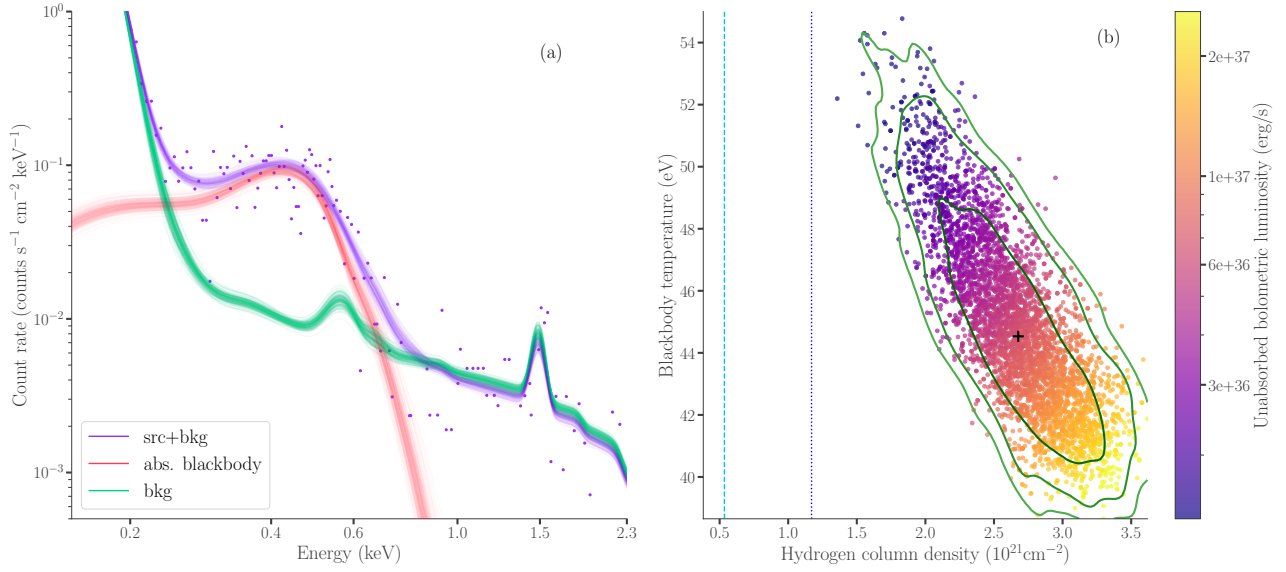


Figure 1 | X-ray temperature and luminosity constraints of [HP99] 159. A 3ML fit of an absorbed blackbody model to the XMM-*Newton* spectrum (a), with a simultaneous fit of the background with linked parameters (see Methods) provides a good fit. Purple symbols and line show the source+background data and model, red the source only, and green the total background. The individual background components are shown in Extended Data (ED) Fig. 4. Panel (b) shows the posterior distribution in the temperature vs. hydrogen column density plane of the spectral fit (a). Each dot represents one model realization. The colour coding represents the unabsorbed bolometric luminosity assuming a distance of 50 kpc. 1σ , 2σ and 3σ confidence contours are overplotted in green. Vertical dashed lines mark the Galactic foreground absorption and the sum of Galactic and total LMC absorption.

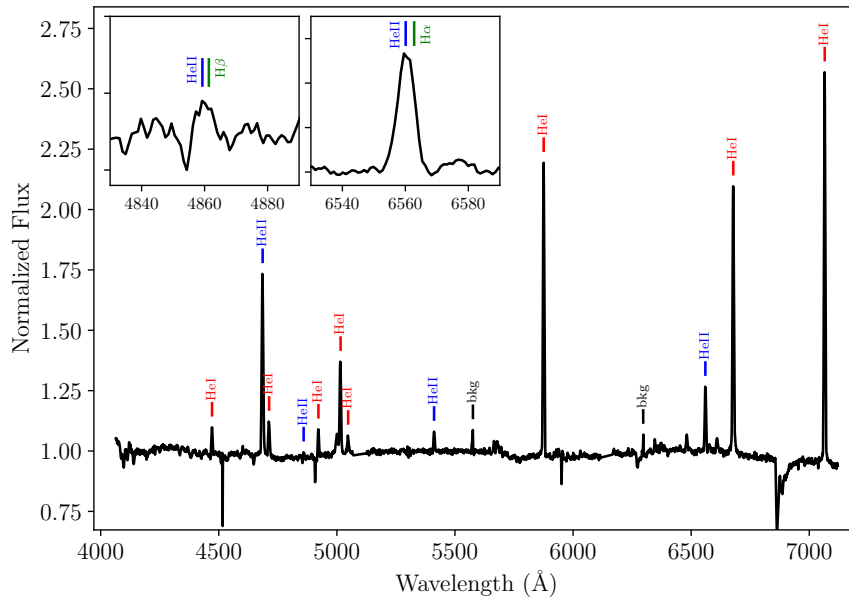


Figure 2 | Low-resolution optical spectrum of [HP99] 159. Flux-normalized optical spectrum taken with the SALT/RSS spectrograph at 2020-08-14 03:44 UT (mid-time of 1200 s exposure), with the major emission lines labeled ('bkg' labels residuals of removing sky lines). The three absorption features apart from the B-band are also due to residuals of sky line removal. The inserts demonstrate that the 4860 Å and 6560 Å lines are due to He II, and not hydrogen.

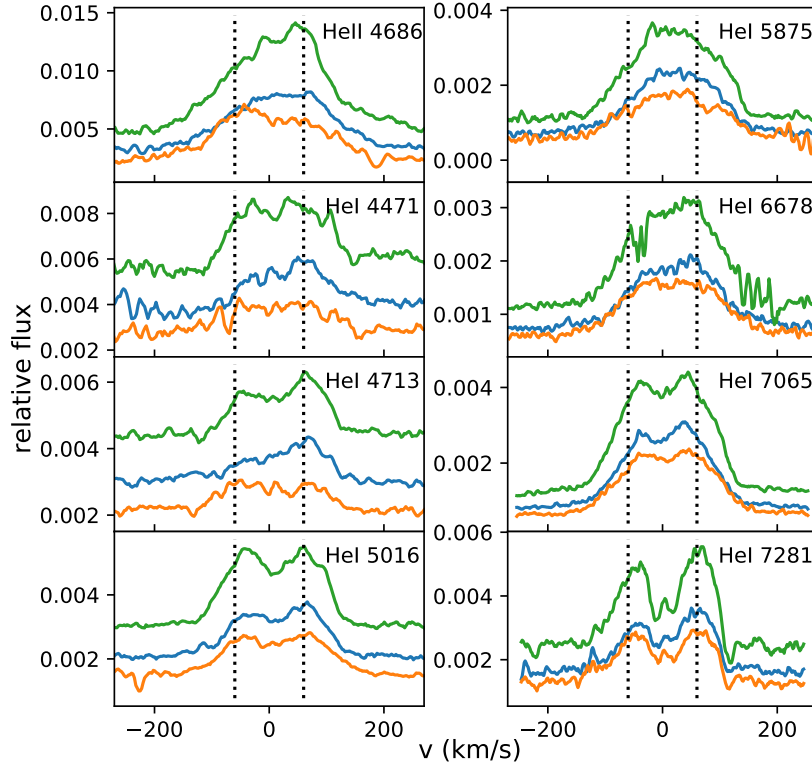


Figure 3 | Double-peak shape of optical emission lines. Flux-normalized optical spectra of different He lines (as labelled on the top right of each panel) taken with the SALT/HRS spectrograph at three different epochs: 15 Sep 2020 (dashed), 5 Oct 2020 (dotted) and 6 Oct 2020 (solid). The peak separation of all major lines is similar, incl. that of He II. The vertical dotted lines indicate a peak separation of $\pm 60 \text{ km s}^{-1}$. The relative variation of blue/red peaks is usually explained as the orbiting hot spot created by the impact of the accretion stream on the outer edge of the accretion disk.

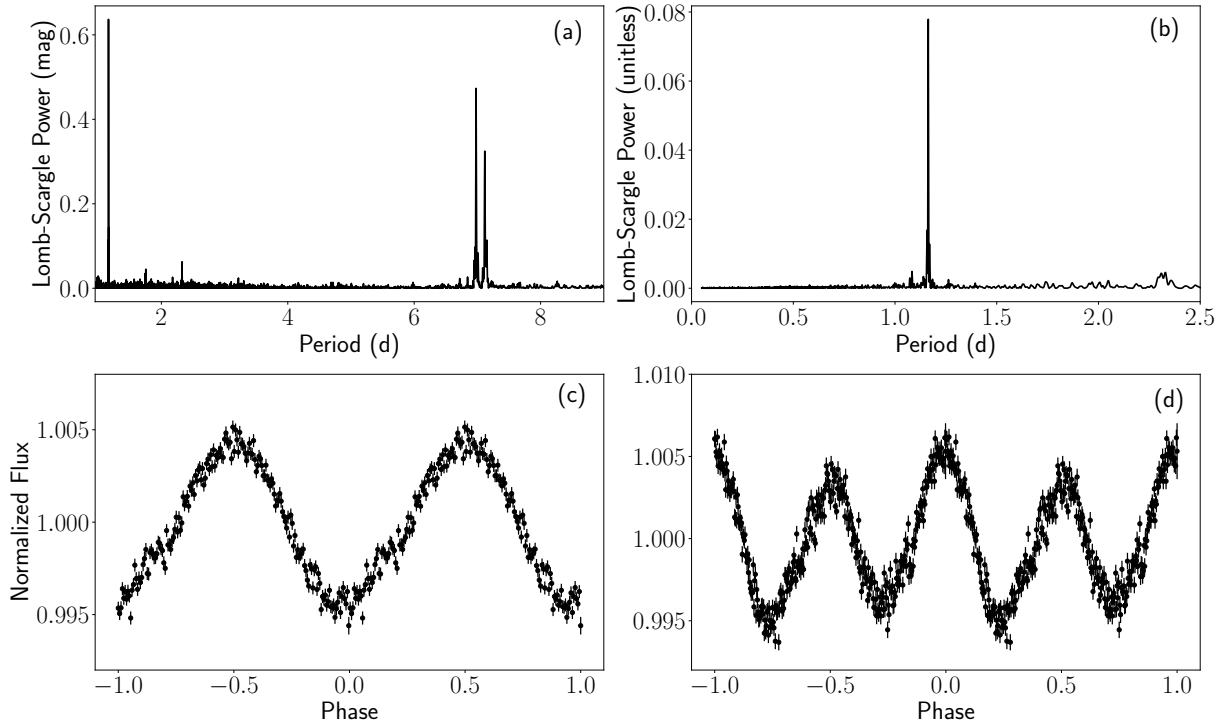


Figure 4 | Optical light variation. Lomb-Scargle periodograms derived from the OGLE I-band data (a) and the TESS data (b). For the interpretation of the OGLE peaks see ED Tab. 1. The TESS data are folded with a period of $P = 1.1635$ days (c) and $P = 2.327$ days (d), corresponding to ephemerides of $2459036.2885297858(14) + 1.1635 \cdot N$ and $2459036.288557(8) + 2.327 \cdot N$ (Barycentric Julian Date), respectively. The error bars for a given point represent the rms error of the individual 10 min data points that went into that one bin. While the Lomb-Scargle periodograms show the highest power at $P = 1.1635$ days, the folded light curve for the longer period (d) has a lower variance and a clear odd-even asymmetry. Lacking phase-resolved spectroscopy for a definite proof, we tentatively identify $P = 2.327$ days as the orbital period of [HP99] 159.

Methods

Optical photometry:

SkyMapper: The optical brightness, measured by SkyMapper³⁶ (not simultaneously) is $g' = 15.82 \pm 0.02$ mag, $r' = 16.04 \pm 0.02$ mag, $i' = 16.41 \pm 0.01$ mag, $z' = 16.59 \pm 0.04$ mag, and after correcting for the Galactic and LMC reddening of $E(B-V) = 0.105$ mag (see below) results in an absolute V-band magnitude of $M_V = -2.8$ mag (assuming a LMC distance¹⁶ of 50 kpc). This is about 5 mag (or a factor $2.5^5 = 100$) brighter than typical disks in high-accretion rate nova-like cataclysmic variables³⁷, and still 15–40x brighter for a face-on disk.

OGLE: The region of our X-ray source was monitored regularly in the V and I bands with the Optical Gravitational Lensing Experiment (OGLE)^{41;42} at a cadence of 1–3 days. Photometric calibration is done via zeropoint measurements in photometric nights, and color-terms have been used for both filters when transforming to the standard VI system. The long-term lightcurve over the 2010–2020 period shows variations by a factor 1.3 and little color variation (see ED Fig. 3). A Lomb-Scargle periodogram identifies a period of $P = 1.1635$ days with the largest power (panels (a) and (b) of Fig. 4), in agreement with $P = 1.163471$ days listed in the EROS-2 catalog of LMC periodic variables (EROS-ID lm0454n2690)⁴⁵. Two other strong peaks at longer periods are aliases (see ED Tab. 1). A much smaller peak is seen at 2.327 days (see below).

MACHO: The source was also covered by the MACHO project⁴³ that monitored the brightnesses of 60 million stars in the Large and Small Magellanic Clouds, and the Galactic bulge between 1992–1999. A visual (4500–6300 Å) and a red filter (6300–7600 Å) were used, the magnitudes of which were transformed to the standard Kron-Cousins V and R system, respectively, using previously determined color-terms⁴⁴.

TESS: The Transiting Exoplanet Survey Satellite⁴⁶ (TESS) is an all-sky transit survey to detect Earth-sized planets orbiting nearby M dwarfs. It continuously observes a given region of the sky for at least 27 days. For sources down to white light magnitudes ≈ 16 mag, TESS achieves $\approx 1\%$ photometric precision in single 10 min. exposures. However, its large plate scale ($21''\text{px}^{-1}$) means that care must be taken wrt. to blended sources.

[HP99] 159 was observed during all of TESS Sectors 27–39 (except Sector 33), i.e. from 2020 July to 2021 June. The analysis of [HP99] 159 is complicated by a 13 mag star at $12''$ distance. Yet, the 1.16 d period found in OGLE data (which resolves these two stars) is clearly visible in a Lomb-Scargle periodogram of the TESS data (Fig. 4) as the strongest peak by far. There is a signal at 2.3268 d, exactly twice of the OGLE period, at a significance of 3σ . While this is marginal, the folded (and re-binned) light curve reveals a clear odd-even effect with smaller variance that leads us to believe that this is the true period, and the strong peak at 1.16 d is likely the first harmonic of this period. The small amplitude difference, at the 0.2%-level, would explain that this is only marginally seen in the TESS periodogram. This period is also

seen in the OGLE periodogram, demonstrating that it is a real feature. The phenomenon of asymmetrical maxima and minima, known in some detached binaries⁴⁷, is unique in interacting binaries, and is especially puzzling given our inferred near face-on geometry.

With the TESS light curve⁴⁸, we also did an independent, more sensitive search at even shorter periods that are inaccessible to OGLE. The TESS light curve was pre-whitened of the 1.16 d period and 25 of its harmonics, and the Fourier transform of the “cleaned” data was calculated. There are no indications for a shorter period down to ≈ 3 hrs (Fig. 4). There is also no signal at 0.538 days. This would be the fundamental period if the 1.16 d period still were an alias with the 1-3 days observing cadence of OGLE. On the other hand, two additional periodicities are found, at $P_1 = 2.635$ h and $P_2 = 1.32$ h, with significances at the 4σ level¹. Given the non-Poissonian nature of the light curve after pre-whitening, we do not consider these two periods, which are not related harmonically, to be significant enough for further investigation.

Swift/UVOT: A 1061 second *Swift* observation was obtained on Aug. 9, 2022, starting at 23:15 UT. While not detected in X-rays (as expected, Fig. 5), we detect [HP99] 159 in all filters of the ultraviolet-optical telescope (UVOT), at AB magnitudes as follows: UVW2 = 15.29 ± 0.04 mag, UVW1 = 15.33 ± 0.04 mag, U = 15.44 ± 0.04 mag, B = 15.73 ± 0.04 mag, V = 15.93 ± 0.05 mag, where the error is the quadratic sum of statistical and systematic error. When added to the (non-simultaneous) measurements on the longer-wavelengths bands (ED Fig. 1), the spectral energy distribution is still well described by a straight powerlaw, extending from 0.2–8 μm , without any sign of the He donor.

SED modelling and extinction correction: The recent reddening map³⁸ of the LMC returns a much smaller reddening than previous estimates. In addition, it provides a combined reddening value for the Galactic foreground and the median LMC-intrinsic value, together with a spread due to variation within the LMC. Instead of trying a somewhat arbitrary extinction correction, we instead forward-fold a powerlaw model to all the photometry from Swift/UVOT, SkyMapper, 2MASS and Spitzer. We fit for the powerlaw slope extinguished by a combination of Milky Way and LMC dust. The powerlaw model fit is very good, and does not require a more complicated spectral model (ED Fig. 1). The best-fit values are a powerlaw slope of $\nu^{1.48 \pm 0.02}$, and E(B-V) values of 0.01 ± 0.01 for Milky Way and 0.14 ± 0.01 for LMC dust. The latter is somewhat larger than the E(B-V)=0.11 mag provided by the LMC reddening map³⁸ (composed of E(I-V)=0.08 mag to the center of the LMC and an additional E(I-V)=0.06 mag towards the far end of the LMC). More importantly, the slope of the spectral energy distribution is different from that expected for a standard accretion disk $F_\nu \propto \nu^{1/3}$ (ED Fig. 1). This is very similar to the SEDs of other supersoft X-ray sources like CAL 83³⁹. The flatter slope has been interpreted as due to reprocessing of the high-luminosity soft X-rays, making the emission ≈ 100 –1000 times larger

¹We assume that the noise is Gaussian and calculate the standard deviation in a 1500-bin window (± 0.1 cycles/day in frequency) around any identified peaks

than the accretion luminosity⁴⁰.

Optical spectroscopy:

Optical spectroscopy of our source was undertaken on the Southern African Large Telescope (SALT). On 14 August 2020 a 1200 s long-slit exposure was obtained using the Robert Stobie Spectrograph (RSS)⁴⁹ in the 4070–7100 Å range (Fig. 2). Three further exposures (2020 Sep. 16, Oct. 06 and 07), using the High Resolution Spectrograph (HRS)⁵⁰, covered the 3700–5500 Å and 5500–8900 Å wavelength ranges. The primary reduction, which includes overscan correction, bias subtraction and gain correction, were carried out with the SALT science pipeline⁵¹.

X-ray analysis:

XMM-Newton: 4XMM J052015.1-654426 was covered serendipitously in a 29 ks XMM-*Newton* observation (ObsId 0841320101, PI: Pierre Maggi) on 2019 September 16/17. The EPIC instruments were operating in full-frame mode, with thin and medium filters for the pn and MOS detectors, respectively. We used the XMM-*Newton* data analysis software SAS version 20.0.0 to process these data. Good time intervals were identified following the method described at <https://www.cosmos.esa.int/web/xmm-newton/sas-thread-epic-filterbackground>. A whole field-of-view lightcurve for single-pixel events with $10000 < PI < 12000$ is created and visually inspected for periods of flaring. A quiescent rate of less than 0.46 cts/s is determined and a GTI file satisfying this condition is created and used to filter the observation. After this filtering and given the off-axis position (8.7 arcmin) of [HP99] 159, its resulting vignettted exposure was ≈ 11.5 ks. The events used for the spectral analysis were filtered with the following expression using the SAS task `evselect`: `'(PATTERN == 0) && (PI in [150 : 15000]) && (FLAG == 0)'`. The SAS task `especget` was used to extract (source and background) events from a circular region with radius $60''$ centered on the position RA (2000.0) = $5^{\text{h}}20^{\text{m}}15^{\text{s}}.4$, Decl. (2000.0) = $-65^{\circ}44'32''$, as well as to calculate RMF and ARF for these events. The same was done with a circular region with radius $110''$ centered on the position RA = $5^{\text{h}}20^{\text{m}}15^{\text{s}}.5$, Decl. = $-65^{\circ}41'11''$, to be used as the background only, after excising two point sources in that region. In order to estimate the spectral parameters of the source, a Bayesian approach was implemented via 3ML^{52;53}. The analysis was restricted to the 0.2–2.3 keV energy band. The background and source contribution to the detected photons were modelled and folded through the appropriate responses to calculate posterior distributions of the spectral parameters. The source was modelled as an absorbed blackbody, using the 3ML models `TbAbs*Blackbody` (no separate abundances are used for the foreground Galactic and the LMC-intrinsic absorption). The background was modelled as a combination of instrumental background (read noise and fluorescence lines) and astrophysical background (Fig. 4), as follows: (i) a Gaussian line with normalisation, line energy and width left free to account for the low-energy noise introduced by the read-out electronics, (ii) a Gaussian line with line energy and width fixed representing the Al-K fluorescent line near 1.5 keV, which is excited by particles in the camera body, (iii) an

unabsorbed APEC model with temperature left free to vary around 0.11 keV accounting for the hot gas of the local bubble, (iv) an APEC model with temperature allowed to vary around 0.22 keV absorbed by the average Galactic hydrogen column in the direction of the source, describing the contribution from the Galactic halo, and (v) a powerlaw with fixed slope of -1.41 , absorbed by the combined hydrogen column of the Galaxy and the LMC in the direction of the source, arising from unresolved AGN. The contribution of the particle background is negligible in our spectral range. The photons in the source extraction region were modelled by adding the source spectrum and the background spectrum, scaled by the ratio of the extraction areas. During the fit of the data, the parameters describing the background models were linked. We obtain the following best-fit values (errors at the 1σ level): $kT = 45 \pm 3$ eV, $N_{\text{H}} = (2.7 \pm 0.4) \times 10^{21}$ cm $^{-2}$, and an unabsorbed bolometric luminosity of $6.8_{-3.5}^{+7.0} \times 10^{36}$ erg/s, see Fig. 1. This implies an emission radius of 3700_{-1900}^{+3900} km, consistent with a white dwarf radius.

Apart from the possibility of the flux-oscillations due to the accretion rate being slightly below the burning rate, two other factors may contribute to the discrepancy of the measured vs. expected X-ray luminosity. First, due to the accretion of pure helium, the burning proceeds via the triple- α process⁵⁴, with $\log T(K) \approx 8.4$ and $\rho \approx 1000$ g cm $^{-3}$ at the burning depth, leading to elevated levels of carbon and oxygen. Convective envelope mixing and subsequent wind ejection of CO-rich matter could lead to noticeable local X-ray absorption in the emission volume. Secondly, Non-LTE model atmospheres (as frequently used for the supersoft phase in post-nova) usually give a higher peak intensity⁵⁵ than blackbody models (at the same temperature). Both effects, if taken into account in future work with improved data, would likely result in a higher X-ray luminosity (and WD radius) than that estimated above.

eROSITA: [HP99] 159 = eRASSU J052015.3-654429 was detected by eROSITA⁵⁶ in each of the survey scans. Until the end of 2021, *eROSITA* scanned the source during five epochs as summarised in Table. 2. The X-ray position was determined from the combined four eRASS surveys to be RA (2000.0) = 05^h20^m15^s.52 and Decl. (2000.0) = $-65^{\circ}44'28''.9$ with a 1σ statistical uncertainty of $0''.6$. The positional error is usually dominated by systematic uncertainties⁵⁷ which presently amount to $5''$ in pointed and $1''$ in scanning observations.

Due to the unprecedented energy resolution (about 56 eV at 0.28 keV), eROSITA data are particularly sensitive to temperature changes of the source. Thus, we decided to perform spectral fitting despite the low number of counts. The spectral analysis was done using the five detectors with the on-chip aluminium filter (telescope modules 1, 2, 3, 4, and 6), avoiding the light leak in the other two detectors⁵⁶. The eSASS⁵⁷ users version 211214 was used to process the data. Only single-pixel events without any rejection or information flag set were selected, using the eSASS task `evtool`. With the eSASS task `srctool`, a circular source region with a radius $100''$, centered on the coordinates RA(2000) = 5:20:16.6, Decl.(2000) = $-65:44:27$ was defined to select source events. A background region of the same size and shape centered on RA(2000) = 05^h21^m09^s.4, Decl.(2000) = $-65^{\circ}46'00''$ was defined, so as to

lie at the same ecliptic longitude as the source region, and hence in the scanning direction of eROSITA. The corresponding ARF and RMF files were created by the same eSASS task. Spectra were constructed by combining all events within the respective regions for each of the 5 epochs of observation. An absorbed blackbody was fitted to each of the spectra using 3ML. The priors of the free parameters were chosen based on the XMM-Newton fit results. For the absorbing column a Gaussian centered at $\mu = 2.7 \times 10^{21} \text{ cm}^{-2}$ and with a width of $\sigma = 0.4 \times 10^{21} \text{ cm}^{-2}$ was used. The prior on kT was a Gaussian with $\mu = 45 \text{ eV}$ and $\sigma = 4 \text{ eV}$, truncated at zero, and the prior on the normalization was a log-normal distribution with $\mu = \log(400)$ and $\sigma = 1$. For the eROSITA data, the background was not modeled due to the low number of counts; rather the data was binned to have at least 1 background photon in every bin and a profile Poisson likelihood was used. For the five epochs we obtain best-fit temperatures of $kT_1 = 42_{-2}^{+3} \text{ eV}$, $kT_2 = 44_{-2}^{+3} \text{ eV}$, $kT_3 = 42_{-2}^{+3} \text{ eV}$, $kT_4 = 42 \pm 2 \text{ eV}$, and $kT_5 = 43 \pm 2 \text{ eV}$. The corresponding fluxes are listed in ED Tab. 2, and shown in ED Fig. 5 together with the fluxes (or limits) of the other X-ray missions.

ROSAT: [HP99] 159 was originally identified¹⁴ in a 8.3 ks ROSAT/PSPC pointed observation (ID: 500053p) of April 1992. We have re-analyzed this observation, and find the source with a vignetting-corrected count-rate of $0.005 \pm 0.001 \text{ PSPC cts/s}$ (40 ± 8 source counts). A blackbody fit with free parameters leads to $kT = 38 \pm 15 \text{ eV}$, $N_{\text{H}} = (0.9_{-0.3}^{+3.2}) \times 10^{21} \text{ cm}^{-2}$ and an unabsorbed bolometric luminosity of $1.3_{-1.0}^{+41.7} \times 10^{36} \text{ erg/s}$. A fit with a fixed, XMM-derived temperature of 45 eV is statistically indistinguishable (due to the very small number of counts and the low energy resolution), and results in an absorption-corrected bolometric luminosity of $1.7_{-1.0}^{+41} \times 10^{36} \text{ erg/s}$, consistent within the errors of the free fit. A fit with fixed, XMM-derived temperature and N_{H} is substantially worse.

[HP99] 159 was not detected during the ROSAT all-sky survey, with a PSPC count rate upper limit of $< 0.012 \text{ cts/s}$. Using the best-fit spectral model of the above ROSAT pointed observation leads to a luminosity limit of $< 2.5 \times 10^{36} \text{ erg/s}$, while using the XMM-derived spectral parameters leads to $< 3.2 \times 10^{37} \text{ erg/s}$. For consistency with the *Einstein* and EXOSAT upper limits we choose to plot the latter value in Fig. 5.

Arguments against an AM CVn interpretation:

The He-dominated accretion disk and the NII and SiII lines (ED Fig. 2) allow the possibility of an AM CVn nature of [HP99] 159. However, a number of reasons argue against this interpretation: (i) AM CVn objects have luminosities⁵⁸ in the range of $10^{30} \dots 10^{32} \text{ erg/s}$. For this to be applicable to [HP99] 159, it would need to be at a distance of order 100 pc. (ii) This is incompatible with the Gaia data, which suggest a minimum distance of 8–12 kpc. (iii) Similarly, all AM CVn stars have large proper motion⁵⁸, of order $0''.5/\text{yr}$, due to their vicinity. This is a factor 100 larger than that of [HP99] 159. (iv) Finally, and most convincing, the velocity shift of all the strong lines clearly indicates LMC membership. At that distance, an AM CVn system is incompatible with the parameters we observe.

Comparison to known similar systems:

To our knowledge, the only other 'known' system of this kind was the progenitor of the He nova V445 Pup⁵⁹. A pre-outburst luminosity of $\log(L/L_{\odot}) = 4.34 \pm 0.36$ would be compatible with a 1.2–1.3 M_{\odot} star burning helium in a shell⁶⁰. No optical spectrum exists of the progenitor; the post-outburst spectra are H-deficient, with the strongest lines being CII and FeII⁶¹. Based on photographic plates taken before the outburst, an optical modulation by a factor of 1.25 and a period of 0.650654(10) days was found, and interpreted as orbital variation of a common-envelope binary⁶². There are three possibilities for the X-ray non-detection: (i) the flux oscillations during burning with phases of low luminosity²⁵, or (ii) the substantial Galactic foreground absorption in the case that the X-ray spectrum was similarly soft as [HP99] 159, or (iii) an only slightly lower temperature as compared to [HP99] 159 which would shift the emission below the X-ray detection window. Thus, the progenitor of the He nova V445 Pup could have been an object similar to [HP99] 159.

Data availability: Data from the ROSAT, XMM-*Newton*, Swift and TESS missions as well as from the OGLE and MACHO projects are publicly available. eROSITA data of the first survey (eRASS1) of HP99-159 will be made public as part of the eRASS1 data release, presently scheduled for March 2023. Data of the subsequent eROSITA surveys (eRASS2 and later) will be made public according to the plan as provided at <https://erosita.mpe.mpg.de/erass/>. The optical spectra taken with the SALT telescope are available at <https://cloudcape.sao.ac.za/index.php/s/g8M1q1ya8e>

Code availability: All data analysis code is publicly available, as referenced in the text.

Additional References

- [36] Onken, C.A., Wolf, C., Bessel, M.S. et al. SkyMapper Southern Survey: Second data release (DR2). *Publ. Astron. Soc. Aust.* **36**, id. e033 (2019)
- [37] Smak, J., On the $M_V - \dot{M}$ relation for accretion disks in cataclysmic binaries. *Acta Astron.* **30**, 317–321 (1989)
- [38] Skowron, D.M., Skowron, J., Udalski A. et al. OGLE-ing the Magellanic System: Optical Reddening Maps of the Large and Small Magellanic Clouds from Red Clump Stars. *Astrophys. J. Suppl. Ser.* **252**, 23 (2021)
- [39] Crampton, D., Cowley, A.P., Hutchings, J.B., Schmidtke, P.C., Thompson, I.B., Liebert, J. CAL 83: A Puzzling X-Ray Source in the Large Magellanic Cloud. *Astrophys. J.* **321**, 745–754 (1987)
- [40] Popham, R., DiStefano, R. Accretion disks in supersoft X-ray sources. *Lect. Notes in Phys.* **472**, 65–72 (1996)
- [41] Udalski, A., Szymanski, M.K., Soszynski, I., Poleski, R. The Optical Gravitational Lensing Experiment. Final Reductions of the OGLE-III Data. *Acta Astron.* **58**, 69–87 (2008)
- [42] Udalski, A., Szymanski, M.K., Szymanski, G. OGLE-IV: fourth phase of the optical gravitational lensing experiment. *Acta Astron.* **65**, 1–38 (2015)
- [43] Alcock, C., Allsman, R.A., Alves, D.R., Axelrod, T.S., Becker, A.C., et al. Calibration of the MACHO Photometry Database. *Publ. Astron. Soc. Pac.* **111**, 1539–1558 (1999)
- [44] Greiner, J., DiStefano, R. X-ray off states and optical variability in CAL 83. *Astron. Astrophys.* **387**, 944–954 (2002)
- [45] Kim, D.-W., Protopapas, P., Bailer-Jones, C.A.L., et al. The EPOCH Project. I. Periodic variable stars in the EROS-2 LMC database. *Astron. Astrophys.* **566**, A43 (2014)
- [46] Ricker, G.R., Winn, J.N., Vanderspek, R. et al. Transiting Exoplanet Survey Satellite (TESS). *J. Astron. Tel., Instr & Sys.* **1**, id. 014003
- [47] Young, A., Nelson, B., Miellbrecht, R. An Old Evolved Binary in the Galactic Halo. *Astrophys. J.* **174**, 27–31 (1972)
- [48] Feinstein, A.D., Montet, B.T., Foreman-Mackey, D. et al. eleanor: An Open-source Tool for Extracting Light Curves from the TESS Full-frame Images. *Publ. Astron. Soc. Pac.* **131**, 094502
- [49] Burgh, E.B., Nordsieck, K.H., Kobulnicky, H.A., et al. Prime Focus Imaging Spectrograph for the Southern African Large Telescope: optical design. *Proc. SPIE* **4841**, 1463–1471 (2003)
- [50] Crause, L.A., Sharples, R.M., Bramall, D.G., et al. Performance of the Southern African Large Telescope High Resolution Spectrograph (HRS). *Proc. SPIE* **9147**, id. 91476T (2014)
- [51] Crawford, S.M. pyhrs: Spectroscopic data reduction package for SALT. *Astrophys. Source Code Lib.* ascl:1511.005 (2015)
- [52] Vianello, G., Lauer, R.J., Burgess, J.M. The Multi-Mission Maximum Likelihood framework (3ML). in *Proc. of the 7th Internatl. Fermi Symp.*, SISSA IFS2017, id. 130

- <https://pos.sissa.it/cgi-bin/reader/conf.cgi?confid=312>, (2017)
- [53] Burgess, J.M., Fleischhack, H., Vianello, G., et al. The Multi-Mission Maximum Likelihood framework (3ML). *Zenodo* 5646954, doi:10.5281/zenodo.5646954 (2021)
- [54] Hansen, C.J., Kawaler, S.D., Trimble, V. *Stellar interiors: Physical principles, structure, and evolution* 2nd ed., New York: Springer, (2004)
- [55] Rauch, T., Werner, K., Non-LTE model atmospheres for supersoft X-ray sources. *Astron. Nachr.* **331**, 146–151 (2010)
- [56] Predehl, P., Andritschke R., Arefiev, V., et al. The eROSITA X-ray telescope on SRG. *Astron. Astrophys.* **647**, A1 (2021)
- [57] Brunner, H., Liu, T., Lamer, G., et al. The eROSITA Final Equatorial Depth Survey (eFEDS). X-ray catalogue. *Astron. Astrophys.* **661**, A1 (2022)
- [58] Ramsay G., Green, M.J., Marsh, T.R., et al. Physical properties of AM CVn stars: New insights from Gaia DR2. *Astron. Astrophys.* **620**, A141 (2018)
- [59] Ashok, N.M., Banerjee, D.P.K., The enigmatic outburst of V445 Puppis - A possible helium nova? *Astron. Astrophys.* **408**, 1007–1015 (2003)
- [60] Woudt, P.A., Steeghs, D., Karovska, M., et al., The Expanding Bipolar Shell of the Helium Nova V445 Puppis. *Astrophys. J.* **709**, 738–746 (2009)
- [61] Iijima, T., Nakanishi, H. Spectroscopic observations of the first helium nova V445 Puppis. *Astron. Astrophys.* **482**, 865–877 (2008)
- [62] Goranskij, V., Shugarov, S., Zharova, A., Kroll, P., Barsukova, E.A. The Progenitor and Remnant of the Helium Nova V445 Puppis. *Perem. Zvezdy* **30**, No. 4 (2009)

Acknowledgements:

RW is supported by the German Science Foundation (DFG) under contract GR1350/17-1, and JMB by the DFG-funded Collaborative Research Center SFB 1258. We thank M. Freyberg (MPE Garching) for discussion of the XMM-*Newton* background modelling, and S. Rappaport (MIT) on TESS time-series analysis. JG is grateful to the Swift team for the rapid scheduling of the UVOT observation.

This work is based on data from eROSITA, the soft X-ray instrument aboard SRG, a joint Russian-German science mission supported by the Russian Space Agency (Roskosmos), in the interests of the Russian Academy of Sciences represented by its Space Research Institute (IKI), and the Deutsches Zentrum für Luft- und Raumfahrt (DLR). The SRG spacecraft was built by Lavochkin Association (NPOL) and its subcontractors, and is operated by NPOL with support from the Max-Planck Institute for Extraterrestrial Physics (MPE). The development and construction of the eROSITA X-ray instrument was led by MPE, with contributions from the Dr. Karl Remeis Observatory Bamberg & ECAP (FAU Erlangen-Nürnberg), the University of Hamburg Observatory, the Leibniz Institute for Astrophysics Potsdam (AIP), and the Institute for Astronomy and Astrophysics of the University of Tübingen, with the support of DLR and the Max-Planck Society. The Argelander Institute for Astronomy of the University of Bonn and the Ludwig Maximilians Universität Munich also participated in the science preparation for eROSITA. The eROSITA data shown here were processed using the eSASS software system developed by the German eROSITA consortium.

This paper utilizes public domain data obtained by the MACHO Project, jointly funded by the US Department of Energy through the University of California, Lawrence Livermore National Laboratory under contract No. W-7405-Eng-48, by the National Science Foundation through the Center for Particle Astrophysics of the University of California under cooperative agreement AST-8809616, and by the Mount Stromlo and Siding Spring Observatory, part of the Australian National University.

Some of the observations reported in this paper were obtained with the Southern African Large Telescope (SALT) under program 2018-2-LSP-001.

This paper includes data collected by the TESS mission. Funding for the TESS mission is provided by NASA's Science Mission Directorate. Resources used in this work were provided by the NASA High-End Computing (HEC) Program through the NASA Advanced Supercomputing (NAS) Division at Ames Research Center for the production of the SPOC data products.

Author contributions

CM, FH, RW and PM analyzed the X-ray data, with JMB providing the 3ML environment. DAHB and IMM obtained the SALT spectra, AU provided the OGLE data, and RJ and RV analyzed the TESS data. JG recognized the He burning nature, and with NL, HR, JB and KW derived the binary system constraints. All authors contributed to the scientific discussion and the writing of the manuscript.

Additional Information

The authors declare no competing interests.

Correspondence and requests for materials should be addressed to JG (jcg@mpe.mpg.de).

Reprints and permissions information is available at www.nature.com/reprints.

Extended Data

Extended Data Table 1 | Peaks in the Lomb-Scargle periodogram of the OGLE data.

Peak No.	Maximum power	P (days)	f (1/days)	1.0 + f (1/days)	1.0 - f (1/days)	f - f _{III} (1/days)
I	0.6367	1.1635	0.8595	1.8595	0.1405	0.7190
II	0.4733	6.9794	0.1433	1.1433	0.8567	2.772×10^{-3}
III	0.3271	7.1171	0.1405	1.1405	0.8595	–

Notes: (i) $1/(f_{II} - f_{III}) = 360.8$ days indicates that these two frequencies are one year aliases of each other. (ii) $1 - f_{III} = 0.859494 \approx f_I$, suggesting that f_I and f_{III} are one day aliases. (iii) Possible shorter periods are: $1/(1+f_{III}) = 0.87680$ days, or $1/(1+f_I) = 0.53778$ days.

Extended Data Table 2 | X-ray Observations of [HP99] 159.

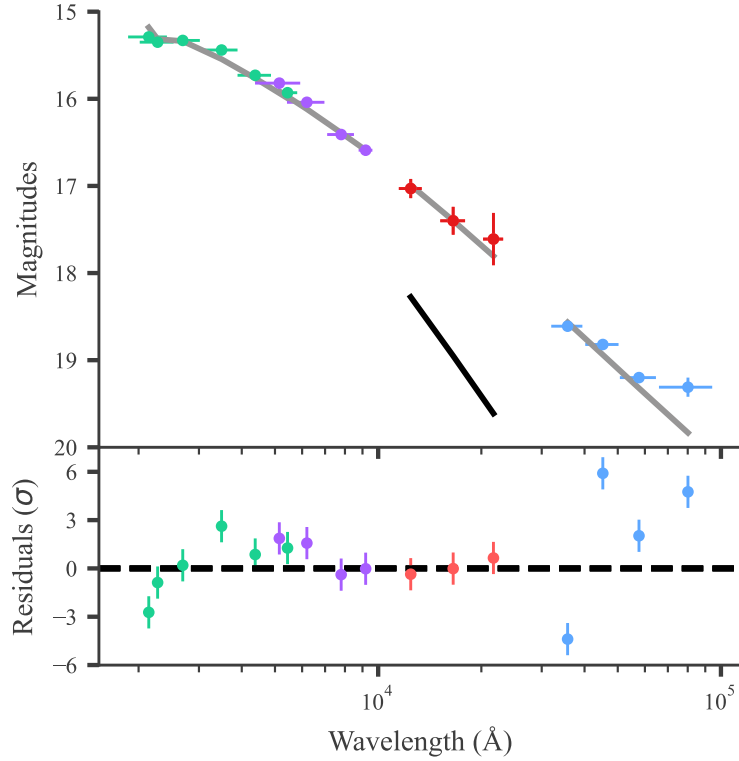
Mission	observation time $T_{start} - T_{stop}$ (UTC)	exposure (ks)	count rate ^a (cts s ⁻¹)	luminosity ^a (erg s ⁻¹)
<i>Einstein</i>	1979-04-12 17:10–1979-04-12 17:50	2.4	<0.01	$<1.8 \times 10^{38}$
EXOSAT	1986-01-21 04:17–1986-01-21 12:00	27.8	< 0.0047	$<9.8 \times 10^{37}$
ROSAT Surv.	1990-07-12 01:33–1990-07-16 02:54	2.4	<0.012	$<3.2 \times 10^{37}$
ROSAT 500053p	1992-04-09 16:10–1992-04-13 19:15	8.3	0.005 ± 0.001	$1.7_{-1.0}^{+41} \times 10^{36}$
XMM-Newton	2019-09-16 18:35–2019-09-17 03:25	28.6	0.056 ± 0.003	$6.8_{-3.5}^{+7.0} \times 10^{36}$
eRASS0/1 ^b	2019-12-11 23:33–2019-12-27 15:33	1.2 ^c	0.10 ± 0.01^d	$7.1_{-2.7}^{+4.5} \times 10^{36}$
eRASS1/2 ^b	2020-06-07 00:57–2020-06-23 20:57	1.0 ^c	0.10 ± 0.01^d	$6.5_{-2.6}^{+4.2} \times 10^{36}$
eRASS2/3 ^b	2020-12-13 14:33–2020-12-28 14:33	0.9 ^c	0.06 ± 0.01^d	$7.1_{-2.7}^{+4.5} \times 10^{36}$
eRASS3/4 ^b	2021-06-11 13:57–2021-06-27 05:57	1.1 ^c	0.09 ± 0.01^d	$6.5_{-2.6}^{+3.9} \times 10^{36}$
eRASS4/5 ^b	2021-12-17 15:33–2021-12-19 15:33	0.1 ^c	0.17 ± 0.08^d	$8.0_{-3.0}^{+4.8} \times 10^{36}$

(a) Count rate is in the 0.2–2 keV band, and luminosity is foreground-absorption corrected.

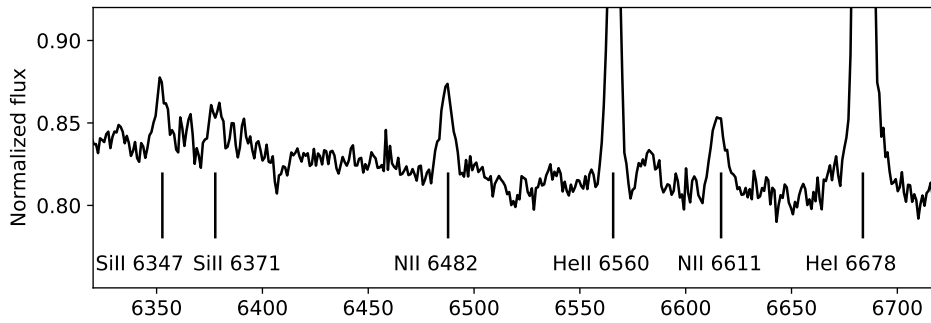
(b) eROSITA test scans from 2019-12-08 to 2019-12-11 are designated as eRASS0. The source position was covered by these test scans and in the early phase of eRASS1. The ≈ 2 week visibility of [HP99] 159 for eROSITA starts at the end of each formal eRASS survey and extends into the start of the following eRASS: we group this into 'epochs' of continuous coverage.

(c) Net exposure per telescope after correcting for vignetting, averaged over the 5 telescope modules used.

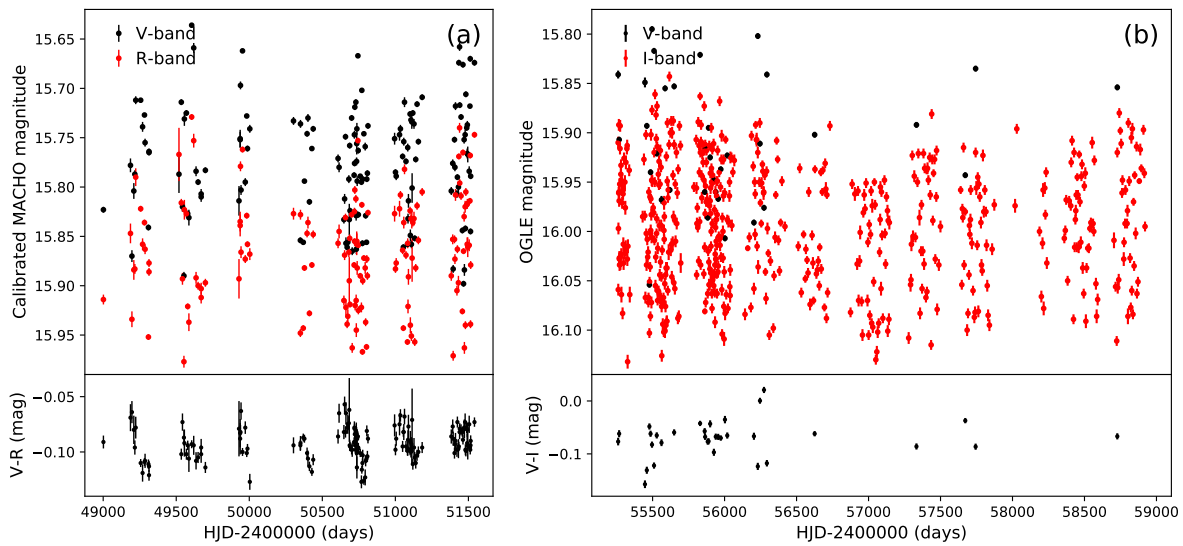
(d) Net source count rate after correcting for vignetting, summed over the 5 telescope modules used.



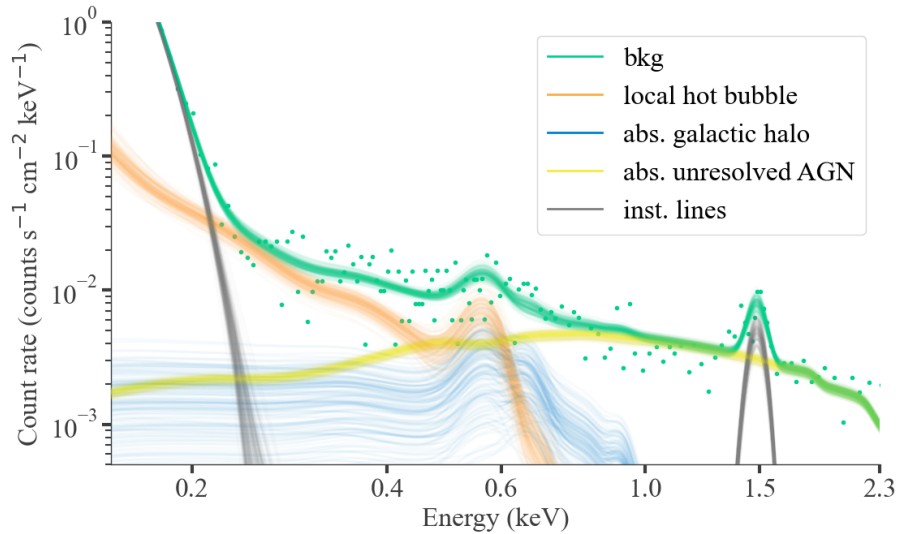
Extended Data Figure 1 | Spectral energy distribution of [HP99] 159. The collection of non-simultaneous photometry of [HP99] 159 from SkyMapper (griz; purple), 2MASS (JHK; red), and Spitzer (IRAC-1 to IRAC-4; blue), together with near-simultaneous 5-filter UV/optical photometry with Swift/UVOT (green). Error bars are at the 1σ level. The extinction has been fit by forward-folding a powerlaw and allowing for the sum of Milky Way and LMC dust extinction curves (best-fit $E(B-V) = 0.14 \pm 0.01$). The orbital variability amplitude of ± 0.15 mag is the likely reason for the scatter in the non-simultaneous data, but has not been included as “systematic” error in the fitting. The slope of the observed spectral energy distribution (grey line; $F_\nu \propto \nu^{1.48 \pm 0.02}$) is clearly different from that expected from a non-irradiated accretion disk (black line: $F_\nu \propto \nu^{1/3}$), consistent with the properties of canonical supersoft X-ray sources⁴⁰.



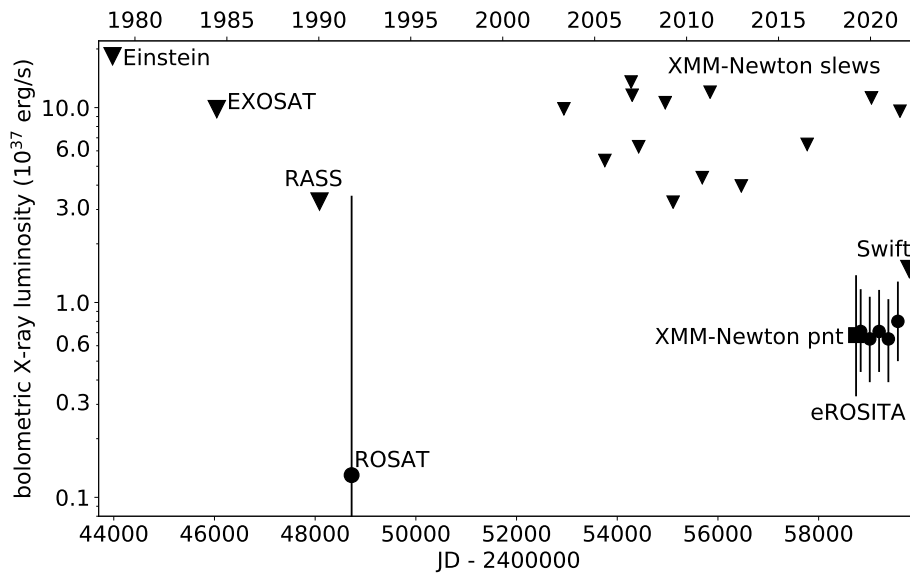
Extended Data Figure 2 | Faint Nitrogen and Silicon lines. Zoom-in of the low-resolution SALT spectrum, showing four of the seven NII and SiII emission lines identified in addition to the He lines.



Extended Data Figure 3 | Optical long-term light-curve of [HP99] 159. MACHO (panel (a); Jan. 1993 – Jan. 2000) and OGLE I-band ((b); Mar. 2010 – Mar. 2020) light curve of [HP99] 159. Error bars are at the 1σ level. The MACHO color has an additional systematic error of ± 0.028 mag. The V -magnitude offset between the two panels is due to the accuracy of the absolute photometric calibration of the MACHO data.



Extended Data Figure 4 | XMM-*Newton* X-ray background modelling. The XMM-*Newton* X-ray background is extracted from a distinct region on the detector, but located close to the source region, and in a first step separately modelled as the sum of four components, as labelled. During the spectral fit of the photons from the source extraction region, the background spectrum is scaled by the ratio of the extraction areas, and the parameters of three of the four background model components were linked; for the read-noise component (steeply falling grey component below 0.3 keV), due to its strong variation over the detector, the parameters were left free.



Extended Data Figure 5 | Long-term X-ray light curve. Compilation of X-ray 2σ upper limits (downward triangles) and detections (filled circles with 1σ error bars) from previous X-ray missions. The upper limits from *Einstein*, EXOSAT and the XMM-*Newton* slews have been computed using <http://xmmuls.esac.esa.int/upperlimitserver/> with $kT=60$ eV and $N_H = 10^{21}$ cm⁻², and then transformed to the best-fit XMM-*Newton* spectral values using WebPIMMS (<https://heasarc.gsfc.nasa.gov/cgi-bin/Tools/w3pimms/w3pimms.pl>).